

An organic quantum battery

James Quach (✉ quach.james@gmail.com)

The University of Adelaide <https://orcid.org/0000-0002-3619-2505>

Kirsty McGhee

University of Sheffield

Lucia Ganzer

Politecnico di Milano

Dominic Rouse

University of St Andrews

Brendon Lovett

University of St Andrews

Erik Gauger

Heriot-Watt University

Jonathan Keeling

University of St Andrews <https://orcid.org/0000-0002-4283-552X>

Giulio Cerullo

Politecnico di Milano <https://orcid.org/0000-0002-9534-2702>

David Lidzey

University of Sheffield <https://orcid.org/0000-0002-8558-1160>

Tersilla Virgili

Politecnico di Milano

Physical Sciences - Article

Keywords: Quantum Mechanics, Superextensive Charging, Quantum Coherent Control, Ultrafast Optical Spectroscopy, Light-matter Coupling

Posted Date: December 11th, 2020

DOI: <https://doi.org/10.21203/rs.3.rs-123919/v1>

License: © ⓘ This work is licensed under a Creative Commons Attribution 4.0 International License.

[Read Full License](#)

An organic quantum battery

J. Q. Quach^{1*}, K. E. McGhee³, L. Ganzer², D. M. Rouse⁴, B. W. Lovett⁴, E. M. Gauger⁵, J. Keeling⁴, G. Cerullo², D. G. Lidzey³, T. Virgili^{2*}

1. Institute for Photonics and Advanced Sensing and School of Chemistry and Physics,
The University of Adelaide, South Australia 5005, Australia

2. Istituto di Fotonica e Nanotecnologia – CNR, IFN - Dipartimento di Fisica,
Politecnico di Milano, Piazza Leonardo da Vinci 32,
20133 Milano, Italy

3. Department of Physics and Astronomy, University of Sheffield, Hicks Building,
Hounsfield Road, Sheffield S3 7RH, U.K.

4. SUPA, School of Physics and Astronomy, University of St Andrews, St Andrews,
KY16 9SS, UK

5. SUPA, Institute of Photonics and Quantum Sciences, Heriot-Watt University, EH14
4AS, UK

*Corresponding authors: quach.james@gmail.com, tersilla.virgili@polimi.it

Quantum batteries harness the unique properties of quantum mechanics to enhance energy storage compared to conventional batteries. In particular, they are predicted to undergo superextensive charging, where batteries with larger capacity actually take less time to charge¹⁻⁴. Up until now however, they have not been experimentally demonstrated, due to the challenges in quantum coherent control. Here we implement an array of two-level systems coupled to a photonic mode to realise a Dicke quantum battery. Our quantum battery is constructed with a microcavity formed by two dielectric mirrors enclosing a thin film of a fluorescent molecular dye in a polymer matrix. We use ultrafast optical spectroscopy to time resolve the charging dynamics of the quantum battery at femtosecond resolution. We

27 **experimentally demonstrate superextensive increases in both charging power and**
28 **storage capacity, in agreement with our theoretical modelling. We find that**
29 **decoherence plays an important role in stabilising energy storage, analogous to the**
30 **role that dissipation plays in photosynthesis⁵. This experimental proof-of-concept is**
31 **a major milestone towards the practical application of quantum batteries in**
32 **quantum⁶ and conventional devices⁷. Our work opens new opportunities for**
33 **harnessing collective effects in light-matter coupling for nanoscale energy capture,**
34 **storage, and transport technologies, including the enhancement of solar cell**
35 **efficiencies⁸⁻¹¹.**

36 Conventional batteries operate on the basis of classical electrochemical principles
37 developed in the eighteenth century. Quantum batteries (QB) represent a new class of
38 energy storage devices that instead operate on distinctly quantum mechanical principles.
39 In particular, they are driven either by quantum entanglement, that reduces the number of
40 traversed states in the Hilbert space compared to (classical) separable states alone^{1-4,12-16},
41 or by cooperative behaviour that increases the effective quantum coupling between
42 battery and source¹⁷⁻¹⁹.

43 System properties can typically be categorised as intensive (i.e. they are
44 independent of the system size, such as density) or extensive (i.e. they grow in proportion
45 to system size, such as mass). QBs exhibit a counter-intuitive property where the charging
46 time is inversely related to the battery capacity. This leads to the intriguing idea that the
47 charging power of QBs is superextensive; that is, it increases faster than the size of the
48 battery. Typically consisting of a collection of N identical quantum subsystems to which
49 an external energy source is applied¹, QBs have been predicted to exhibit superextensive
50 charging rate density (charging rate per subsystem) that scales as N or \sqrt{N} in the
51 thermodynamic limit⁴; therefore, the total charging rate grows faster than the system size.
52 If experimentally verified, this would have important implications for energy storage and
53 capture technologies. However, there are challenges in engineering the precise

54 environment in which such behaviour can occur, and in monitoring the ultrashort charging
55 time scales.

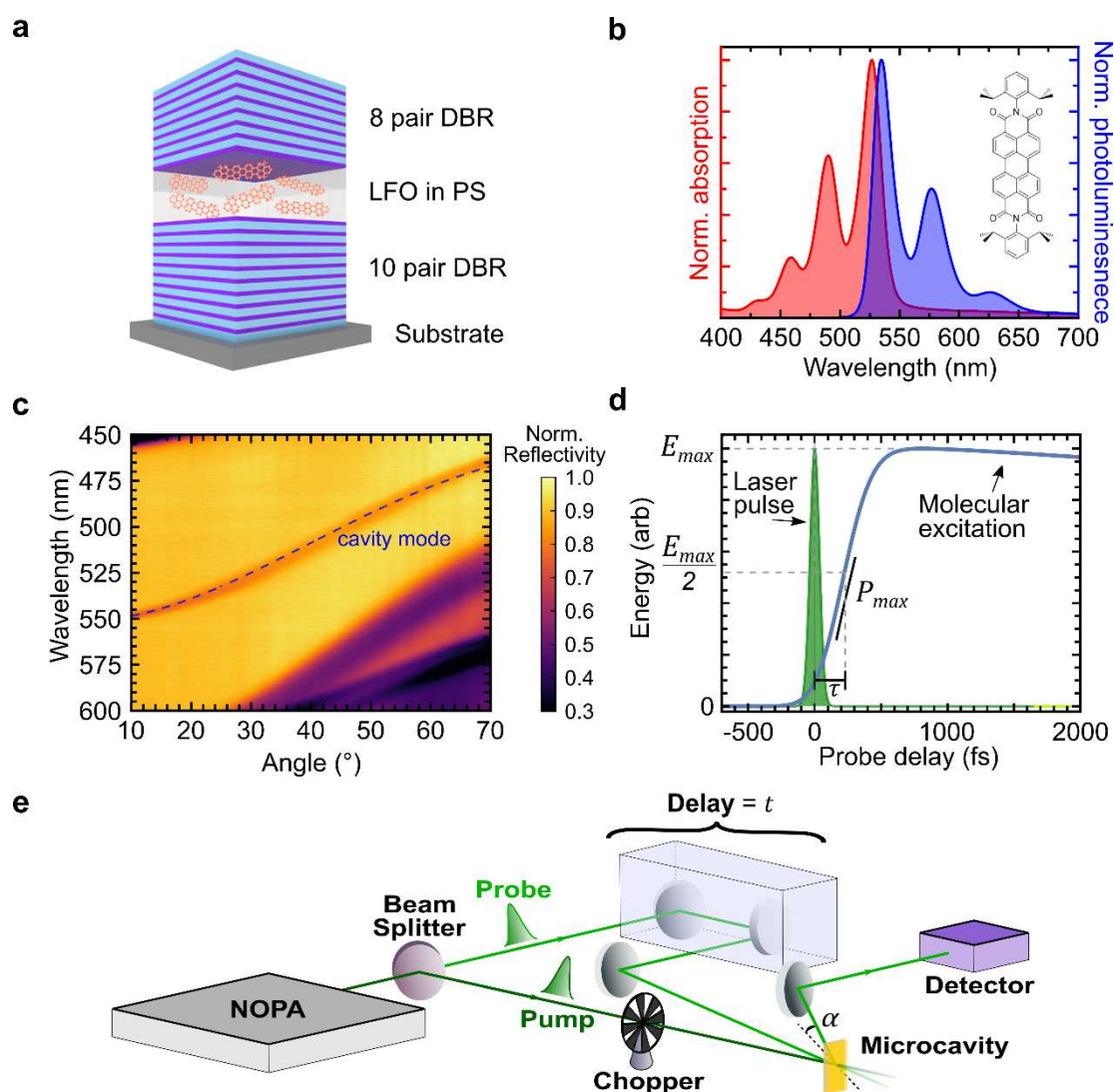
56 Here we experimentally realise a Dicke QB¹⁹ (DQB) using an organic
57 semiconductor as an ensemble of two-level systems (TLSs) coupled to a confined optical
58 mode in a microcavity. This provides a practical version of the DQB which uses the
59 optical cavity mode to induce collective coupling between light and the molecules. In this
60 device, constructive interference of different absorption processes leads to enhanced
61 transition rates, analogous to superradiant emission²⁰ and superabsorption²¹. We
62 demonstrate how dissipation plays a crucial role in the performance of our DQB. In a
63 closed system, the coherent effects that lead to fast charging can also lead to subsequent
64 fast discharging. In our open noisy system, dephasing enables a *ratchet* effect, where
65 excited states are capable of absorbing but not losing energy²², thereby retaining the
66 stored energy until it can be used.

67 **Quantum battery structure**

68 The fabricated DQBs consist of a thin layer of a low-mass molecular semiconductor
69 dispersed into a polymer matrix that is deposited by spin-coating and positioned between
70 two dielectric mirrors, forming a microcavity as illustrated schematically in Fig. 1a (see
71 Methods section for fabrication details). Organic semiconductors are particularly
72 promising for many applications as the high oscillator strength and binding energy of
73 molecular excitons means that light can be absorbed efficiently and excitons can exist at
74 room temperature²³. The organic semiconductor used in this study was the dye Lumogen-
75 F Orange (LFO), whose chemical structure is shown in Fig. 1b. The normalised
76 absorption and photoluminescence spectra for LFO dispersed at 1% concentration by
77 mass in a polystyrene (PS) matrix are shown in Fig. 1b. By diluting the LFO, we reduce
78 intermolecular interactions that lead to emission quenching, producing a high
79 photoluminescence quantum yield of around 60% at low concentration (see Extended

80 Data Fig. 1). The absorption peak at 526 nm and the emission peak at 534 nm correspond
 81 to the 0-0 transition, i.e. an electronic transition to and from the lowest vibrational state.
 82 Operating around the 0-0 transition, the LFO molecules can reasonably be considered as
 83 a TLS. We prepared samples with 0.5%, 1%, 5%, and 10% concentrations, as these are
 84 representative of the optimal operating regimes - further increases in concentration lead
 85 to quenching, and signals from lower concentrations are indiscernible from noise. The
 86 absorption and photoluminescence spectra for the 0.5%, 5% and 10% concentrations are
 87 given in Extended Data Fig. 2.

88



89

90 **Fig. 1 Schematics of the LFO microcavity and experimental setup.** (a) Microcavity consisting
 91 of Lumogen-F Orange (LFO) dispersed in a polystyrene (PS) matrix between distributed Bragg

92 reflectors (DBRs). **(b)** Normalised absorption (red) and photoluminescence (blue) spectra for 1%
93 concentration LFO film, with the molecular structure shown in the inset. We operate near peak
94 absorption/photoluminescence. **(c)** Angle-dependent reflectivity of the 1% cavity, with a fit for
95 the cavity mode shown by the blue dashed line. **(d)** A laser pump pulse excites the LFO molecules.
96 The energetics of the molecules are then measured with probe pulses delayed by time t , from
97 which we can ascertain the peak energy density (E_{\max}), rise time (τ), and peak charging power
98 (P_{\max}). **(e)** The experimental setup for ultrafast transient reflectivity measurements. The output of
99 a non-collinear optical parametric amplifier (NOPA) is split to generate pump (dark green) and
100 probe (light green) pulses. A mechanical chopper is used to modulate the pump pulse to produce
101 alternating pump-probe and probe-only pulses.

102

103 The optical microcavities fabricated support cavity modes whose energy is
104 determined by the optical-thickness of the LFO layer and the penetration of the optical
105 field into the cavity mirrors²⁴. The confined photon field drives coherent interactions with
106 the molecules, which underpin the collective effects of the DQB. The LFO concentration
107 dictates the operating coupling regime, with the 0.5% and 1% LFO cavities operating in
108 the weak coupling regime, the 5% in the intermediate coupling regime, and the 10% in
109 the strong coupling regime (see Extended Data Fig. 2 and discussion in Methods).

110 **Experimental setup**

111 The charging and energy storage dynamics of the DQB were measured using ultrafast
112 transient-absorption (TA) spectroscopy²⁵, allowing femtosecond charging times to be
113 measured. In this technique, we excite the DQB with a pump pulse, and then measure
114 the evolution of stored energy (corresponding to the number of excited molecules) with
115 a second probe pulse, delayed by time t (Fig. 1d). The probe pulse is transmitted through
116 the top distributed Bragg reflector (DBR) of the cavity, and the reflection from the bottom
117 DBR is measured. The differential reflectivity induced by the pump-pulse is given by

$$\frac{\Delta R}{R}(t) = \frac{R_{ON}(t) - R_{OFF}}{R_{OFF}}, \quad (3)$$

118 where R_{ON} (R_{OFF}) is the probe reflectivity with (without) the pump excitation. Note that
 119 control films are measured under differential transmittivity $\Delta T / T$.

120 In our experimental setup (shown schematically in Fig. 1e), TA measurements
 121 were performed in a degenerate, almost collinear configuration. Pump and probe pulses
 122 were generated by a broadband non-collinear optical parametric amplifier (NOPA)²⁶ and
 123 spanned the wavelength range 500 to 620 nm with a nearly transform-limited sub-20-fs
 124 duration (further details in Methods). An optical delay line was used to control the probe
 125 delay time, and a mechanical chopper was used to modulate the pump pulse, providing
 126 alternating probe-only and pump-probe pulses, allowing us to measure pump-induced
 127 absorption changes. Measurements at different molecular concentrations were performed,
 128 adjusting the pump fluence in order to maintain an approximately constant photon density
 129 (i.e. pump photons per LFO molecule) $r = kN_{\gamma}/N$, where N is the total number of
 130 molecules in the excitation volume, N_{γ} is the total number of pump laser photons, and k
 131 is the fraction of them that actually reach the active layer of DQB. We estimate from the
 132 reflectivity data that only 6% to 8% of the initial pump excitation enters the cavity.

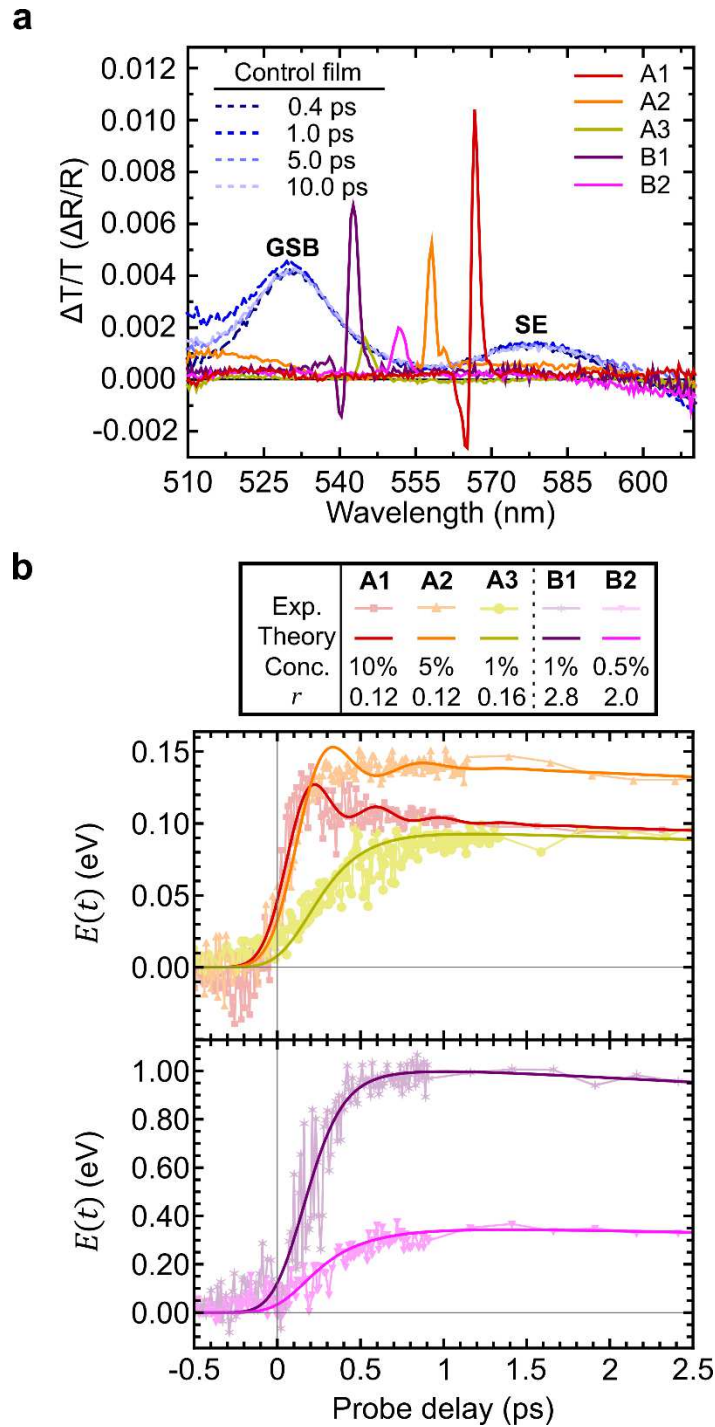
133 **Results**

134 We first show that ultrafast TA spectroscopy can monitor the population of
 135 excited molecules, even in a cavity, by comparing the control film and the DQB spectra
 136 as shown in Fig. 2a. The control film $\Delta T/T$ spectra are shown for various probe delays
 137 (0.4 to 10 ps), and the $\Delta R/R$ spectra of the DQBs are shown at a delay of 1.25 ps. The
 138 control film spectra show two positive bands around 530 and 577 nm, which both reflect
 139 excited state populations. By comparison with the spectra in Fig.1b, we attribute the 530

140 nm band to ground state bleaching (GSB) – i.e. suppression of absorption due to
 141 molecules already being in their excited state. The 577 nm band instead corresponds to
 142 stimulated emission (SE) by excited molecules. For each of the DQB spectra, we have a
 143 single prominent peak, which corresponds to the transient signal filtered by the cavity
 144 mode. This implies that the time-dependent transient reflectivity signal is proportional to
 145 the change in the number of excited molecules created by the pump²⁷, i.e. $\frac{\Delta R}{R}(t) \propto N_{\uparrow}(t)$.
 146 By normalising the peak value of $\Delta R/R$ to $\hbar\omega N_{\uparrow}^{\max}/N$, we can directly relate $\frac{\Delta R}{R}(t)$ to
 147 the temporal behaviour of the stored energy density of the DQB: $E(t) = \hbar\omega N_{\uparrow}(t)/N$,
 148 where ω is the molecular electronic transition frequency (taken to be equal to the cavity
 149 frequency). N_{\uparrow}^{\max} is calculated through theoretical modelling. We also note that two of
 150 the DQB spectra show a negative $\Delta R/R$ band, which results from the change in the
 151 refractive index induced by the pump pulse²⁸.

152 Figure 2b shows the experimental values for the time-dependent stored energy
 153 density in the DQBs. In all DQBs studied, the energy density undergoes a rapid rise
 154 followed by slow decay. The timescale of the rapid rise varies with concentration. We
 155 adjust the laser power to fix photon density r across comparable DQB samples, and
 156 compare behaviour with different LFO concentrations. We found that to achieve a
 157 sufficiently high signal-to-noise ratio, it was not possible to compare all DQBs at the same
 158 r value; instead, a constant r value was maintained for matched DQB samples.
 159 Specifically, measurements were made on DQBs with LFO concentrations of 10%, 5%
 160 and 1% with approximately constant $r \simeq 0.14$ (respectively labelled A1, A2, and A3),
 161 and 1% and 0.5% with $r \simeq 2.4$ (labelled B1 and B2).

162



163

164

165

166

167

168

Fig. 2 Experimental demonstration of the superextensive charging of the Dicke quantum battery. (a) Differential-transmittivity ($\Delta T/T$) spectra for the control film at various probe delay times, and the differential-reflectivity ($\Delta R/R$) spectra for the DQBs at 1.25 ps probe delay. (b) Temporally resolved energy density of the DQBs. A1, A2 and A3 label results for DQBs containing LFO at concentrations of 10%, 5% and 1%, as the ratio of pump photons to

169 molecules is kept approximately constant at $r \simeq 0.14$. B1 and B2 label measurements for LFO at
 170 concentrations of 1% and 0.5%, with $r \simeq 2.4$. The use of two different r values was necessary to
 171 achieve a sufficiently high-signal-to-noise ratio. Points mark the experimental data, while
 172 continuous solid lines are the results of the theoretical model.

173

174 Overlaying the experimental data are the corresponding theoretical predictions
 175 (see Theoretical Model section), convolved with a Gaussian response function of ~ 120 fs
 176 full-width-at-half-maximum, to account for both the instrument response time (~ 20 fs)
 177 and the cavity photon lifetime (which was extracted from the linewidth of the cavity
 178 mode). Although the signal-to-noise ratio is not sufficiently high to discern the predicted
 179 oscillatory behaviour in the A1 and A2 data, there is otherwise good agreement between
 180 the experimental data and the corresponding theoretical model.

181 To obtain the energetic dynamics of the DQBs, we take away the response
 182 function from the theoretical fit, as shown in Extended Data Fig. 3. Extended Data Table
 183 1 summarises the rise time or the time to reach half maximum energy (τ), the battery
 184 capacity or peak stored energy density (E_{\max}), and the battery charging rate or peak
 185 charging power density [$P_{\max} = \max(dE/dt)$] of the data presented in Figs. 2b and c.
 186 The data shows that τ decreases with N , whilst E_{\max} and P_{\max} increase with N . Recalling
 187 that E_{\max} and P_{\max} are the stored energy and charging power *per molecule*, this indicates
 188 superextensive behaviour. The scaling with N is not the same across all experiments. We
 189 define an effective power-law scaling of observables $q_i \in \{\tau, E_{\max}, P_{\max}\}$ in experiment i
 190 by the relation $q_i/q_j = (N_i/N_j)^{f_q}$. As all our observables are intensive (i.e. densities),
 191 $f_q > 0$ indicates superextensive behaviour, $f_q = 0$ indicates extensive, and $f_q < 0$

192 subextensive behaviours. Table 1 gives the observed values of f_q . The different values of
 193 f_q are explained in the Theoretical Model section.

194 Our results demonstrate that as the size of the DQB increases, its charging time
 195 remarkably decreases whilst also increasing its stored energy density. This means that it
 196 takes less time to charge a single N -molecule DQB, than it would to charge N single-
 197 molecule DQBs, even if the latter were charged simultaneously. Furthermore, one DQB
 198 with N molecules would store more energy than N DQBs, where each DQB contained a
 199 single molecule. These superextensive DQB properties are the key experimental findings
 200 of our work, and are supported by the theoretical modelling presented in the next section.

201

Exp.	f_τ	$f_{E_{\max}}$	$f_{P_{\max}}$
A1/A2	-0.46	0.07	0.69
A2/A3	-0.40	0.62	1.08
B1/B2	-0.39	1.73	2.14

202 **Table 1: Observed subextensive and superextensive scaling behaviours in rise-time, stored**
 203 **energy, and charging power.** Power-law exponent f_q (see text) for observable $q \in$
 204 $\{\tau, E_{\max}, P_{\max}\}$, where $f_q > 0$, $f_q = 0$, $f_q < 0$ indicates superextensivity, extensivity, and
 205 subextensivity, respectively. Table values indicate that charging time τ is subextensive, whilst
 206 stored energy E_{\max} and charging power P_{\max} are superextensive. The first column indicates the
 207 corresponding experiments.

208 Theoretical Model

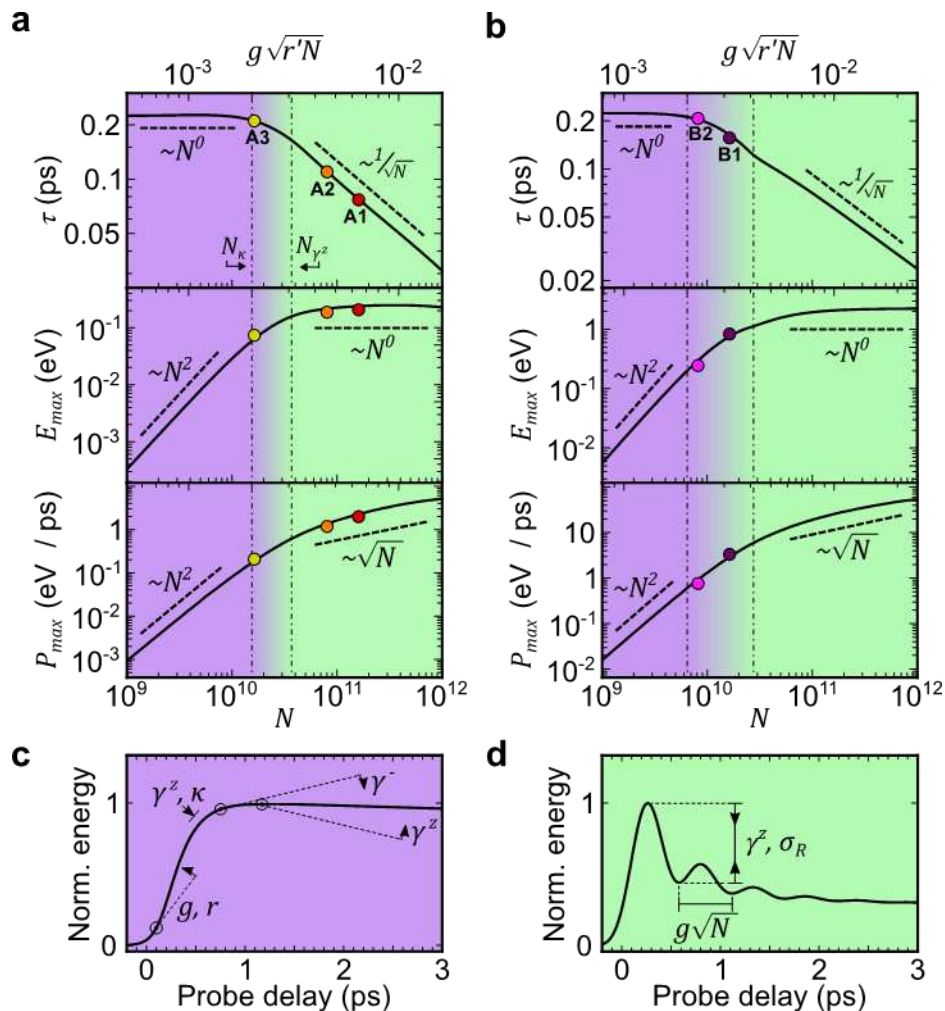
209 The experimental dynamics of the DQBs can be reproduced by modelling, with the
 210 Lindblad master equation (LME), the N TLSs in an optical cavity with light-matter
 211 coupling strength g , a driving laser with a Gaussian pulse envelope and peak amplitude

212 η_0 , and three decay channels corresponding to the cavity decay (κ), TLS dephasing (γ^z),
 213 and TLS relaxation (γ^-). To solve this many-body LME, we make use of the cumulant
 214 expansion²⁹⁻³¹, with model parameters given by a chi-squared minimisation of the
 215 experimental data. Experimental uncertainties are estimated from the point-to-point
 216 variance of the data. Further details can be found in the Methods and Supplementary
 217 Information.

218 From our cumulant expansion simulations, we show how τ , E_{\max} , and P_{\max} vary
 219 as a function of N in Fig. 3a and b. The interplay amongst the decay channels, driving
 220 laser, and cavity couplings give rise to a rich set of behaviour. We identify three regimes:
 221 decay-dominated at small N , and coupling-dominated at large N , along with a crossover
 222 regime between them. Figures 3c and d show the typical time dependence of the DQB in
 223 decay-dominated and coupling-dominated regimes, indicating how the model parameters
 224 affect the dynamics. In particular, the presence of the decay channels gives rise to ratchet
 225 states which are capable of absorbing but not emitting light²², thereby allowing the energy
 226 to be stably stored in the battery. See Methods and Supplementary Information for further
 227 discussion on the operating regimes. Figure 3 is augmented with an animation of how the
 228 energetic dynamics of the DQB changes with N (see Supplementary Video).

229 Figures 3a and b provide an explanation for the scaling factors in Table 1.
 230 Specifically, A1 and A2 operate in the coupling-dominated regime, where τ scales
 231 slightly less than $N^{-1/2}$, E_{\max} scales slightly more than N^0 , and P_{\max} scales slightly more
 232 than $N^{1/2}$. For the region between A2 and A3, the average scaling of τ falls between N^0
 233 and $N^{-1/2}$, E_{\max} between N^2 and N^0 , and P_{\max} between N^2 and $N^{1/2}$. As A2 is further
 234 in the coupling-dominated regime than A3 is in the decay-dominated regime, the average
 235 scaling values between A2 and A3 are skewed towards the coupling-dominated scalings.

236 B1 and B2 operate in the cross-over regime, with average scaling factors that are between
 237 the decay-dominated and coupling-dominated scalings, as reflected in Table 1.
 238



239

240 **Fig. 3: Operating regimes of the quantum batteries.** (a) and (b) show the theoretical
 241 model (solid line) for $r = 1.4$ and 2.4 , respectively. We show three operating regimes: decay-
 242 dominated (purple), coupling-dominated (green), and a decay-coupling-crossover regime. The
 243 decay-dominated regime is bounded by $N_\kappa < \kappa^2/g^2r'$, and the coupling-dominated regime
 244 is bounded by $N_{\gamma^z} > \gamma^{z2}/g^2r'$, where $r' = \max(1, r)$. The coloured dots indicate where the
 245 experiments sit on these curves. The uncertainty in N is 10%, which is smaller than the dot size.
 246 (c) qualitatively depicts the effects of the model parameters in shaping the dynamics in the decay-

247 dominated regime. (d) qualitatively depicts the effects of the additional model parameters in
248 shaping the dynamics in the coupling-dominated regimes.

249 **Summary**

250 We have demonstrated the operation of an open-system DQB driven by an external
251 coherent light source and shown regimes of superextensive behaviour using ultrafast
252 optical spectroscopy. We have provided direct experimental evidence of superextensive
253 energy storage capacity and charging in the decay- and coupling-dominated regimes. Our
254 realisation of a prototype QB highlights the fact that purely closed unitary dynamics is
255 insufficient for realising a practical QB. The retention of energy requires finely-tuned
256 decoherence processes, allowing the battery to charge quickly and yet discharge much
257 more slowly. Our observation of such ratchet-type behaviour shows that realistic noisy
258 environments are crucial for the implementation and application of useful QBs.

259 A prime example of how QBs could be applied to enhance existing technologies
260 is in the field of solar energy conversion. The efficient solar energy harvesting that
261 happens in natural photosynthesis derives from the intricate interplay of coherent and
262 dissipative dynamics that we also exploit in our QB design, and we may learn further
263 lessons from nature for improving QBs. Further, QBs could be made to charge more
264 efficiently by surrounding them with antenna molecules that capture light through
265 superabsorption^{21,32,33}. Since the working principle of DQBs is closely related to
266 superabsorbing behaviour, it may be possible to generate even faster charging by using
267 environmental engineering and control approaches. These could keep the QB operating
268 in the range of higher-lying energy states that are associated with maximum absorption
269 enhancement, i.e. near the mid-point of the Dicke ladder²². Although our QB was charged

270 by a coherent laser source, it opens a pathway for charging with incoherent sunlight,
271 offering an exciting new approach to the design of solar-cell technology.

272

273 **Methods**

274 **Quantum battery fabrication**

275 The microcavities constructed consist of a thin layer of LFO (Kremer Pigmente) dispersed
276 in a PS (Sigma-Aldrich, average molecular weight ~ 192,000) matrix. The bottom DBR
277 consisted of 10 pairs of SiO₂/Nb₂O₅ and were fabricated using a mixture of thermal
278 evaporation and ion-assisted electron beam deposition by Helia Photonics Ltd. Solutions
279 of LFO dissolved in 25 mg/mL PS in dichloromethane were prepared at 0.5%, 1%, 5%,
280 and 10% concentration by mass. Each LFO solution was then spin-coated on top of the
281 bottom DBR to produce a thin film with an approximate thickness of 185 nm. An 8-pair
282 DBR was then deposited on top of the LFO layer using electron beam deposition. With
283 this pair of mirrors, the reflectivity was >99% in the spectral region of interest³⁴.

284 The diluted molecules are expected to be isolated at low concentration 0.1 – 1%,
285 but at higher dye concentrations, the 0-0 emission transition red-shifts by a few nm and
286 the second peak increases in intensity due to aggregation of the dye molecules. This is
287 evident in Extended Data Fig. 2a and b, with additional broader features observed at
288 longer wavelengths, which we assign to intermolecular states such as excimers.

289 The 0.5% and 1% cavities lie in the weak-coupling regime, i.e. no polaritonic
290 splitting could be seen in the cavity reflectivity spectrum, as shown in Extended Data Fig.
291 2. For the 5% cavity, we see a weak anti-crossing feature in the reflectivity spectrum (a
292 small kink near the crossing), indicating operation in the intermediate coupling regime.
293 The 10% cavity operated in the strong-coupling regime, showing a Rabi splitting of

294 around 100 meV around the 0-0 transition (along with intermediate-coupling between the
295 cavity mode and the 0-1 transition).

296 Extended Data Fig. 4 shows a transfer matrix simulation of the electric field
297 distribution of the 1% cavity (the cavities exhibit similar distributions).

298 **Pump-probe spectroscopy**

299 Probe and pump pulses were generated by a broadband non-collinear optical parametric
300 amplifier (NOPA). The NOPA was pumped by a fraction (450 μ J) of the laser beam
301 generated by a regeneratively amplified Ti:Sapphire laser (Coherent Libra) producing 100
302 fs pulses at 800 nm at a repetition rate of 1 kHz. A pair of chirped mirrors were placed at
303 the output of the NOPA to compensate for temporal dispersion, and by using 7 ‘bounces’
304 we were able to generate pulses with a temporal width below 20 fs. The laser beam was
305 then split by a beam-splitter, with the probe being delayed via a translation stage and the
306 pump being modulated mechanically using a chopper at 500 Hz.

307 **Number of molecules in film**

308 To determine the number of LFO molecules in the DQBs, we first determined the
309 absorption cross-section of a single LFO molecule, σ_{LFO} . The transmission spectrum of a
310 0.1% solution of LFO in 25 mg/mL PS/dichloromethane in a 1 mm thick cuvette was
311 measured using a Horiba Fluoromax 4 fluorometer with a xenon lamp. The absorption
312 coefficient ($\alpha = n\sigma_{LFO}$) of the 0-0 transition was then calculated using the relation $T /$
313 $T_0 = e^{-\alpha d}$, where T/T_0 is the fractional transmission of the xenon lamp at the 0-0
314 transition, d is the cuvette thickness, n is the number density of absorbing molecules in
315 solution per unit volume, and σ_{LFO} is the absorption cross-section of a single LFO

316 molecule³⁵. Using the known value of n for this solution, σ_{LFO} was calculated as
 317 $3.3 \times 10^{-16} \text{ cm}^2$.

318 The transmission of the 10% LFO concentration in film was then measured to
 319 obtain α and hence n (number density of molecules in the cavity active layer), using the
 320 measured value of σ_{LFO} , with d (film thickness) measured using a Bruker DektakXT
 321 profilometer. This value was then multiplied by the area of the laser beam and d to obtain
 322 N . Here we assume a uniform distribution in the active layer. N for other concentrations
 323 were scaled accordingly.

324 Lindblad master equation

325 The open driven system of the experiment is modelled with the Lindblad master equation,

$$\dot{\rho}(t) = -\frac{i}{\hbar} [H(t), \rho(t)] + \sum_{j=1}^N (\gamma^z \mathcal{L}[\sigma_j^z] + \gamma^- \mathcal{L}[\sigma_j^-]) + \kappa \mathcal{L}[a], \quad (2)$$

326 where $\rho(t)$ is the density matrix and $\mathcal{L}[O] \equiv O\rho O^\dagger - \frac{1}{2}O^\dagger O\rho - \frac{1}{2}\rho O^\dagger O$ is the
 327 Lindbladian superoperator. a^\dagger and a are the cavity photon creation and annihilation
 328 operators, and $\sigma_j^{x,y,z}$ are the Pauli spin matrices for each molecule, with the raising and
 329 lowering spin operators defined as $\sigma_j^\pm = \sigma_j^x \pm i\sigma_j^y$. There are three decay channels
 330 corresponding to the cavity decay (κ), dephasing (γ^z), and relaxation rate (γ^-) of the
 331 individual TLSs. The Hamiltonian for the LFO molecules in cavity is modelled as a
 332 collection of non-interacting TLSs with characteristic frequency ω equal to that of the
 333 cavity mode, and resonantly coupled to the cavity with strength g . The molecules are
 334 driven by a laser described by a Gaussian pulse envelope $\eta(t) = \frac{\eta_0}{\sigma\sqrt{2\pi}} e^{-\frac{1}{2}\left(\frac{t-t_0}{\sigma}\right)^2}$, and a
 335 carrier frequency ω_L . We work in the frame of the laser carrier frequency, and so write

$$H(t) = \hbar\Delta a^\dagger a + \sum_{j=1}^N \left[\frac{\hbar\Delta}{2} \sigma_j^z + g(a^\dagger \sigma_j^- + a \sigma_j^+) \right] + i\hbar\eta(t)(a^\dagger - a), \quad (3)$$

336 where $\Delta = \omega - \omega_L$ is the detuning of the cavity frequency from the laser driving
 337 frequency. The LFO molecules are initially in the ground state, and the laser is on-
 338 resonance ($\Delta = 0$).

339 **Cumulant expansion**

340 The energy density of the cavity containing identical molecules with transition energy ω
 341 is $E(t) = \frac{\hbar\omega}{2} [\langle \sigma^z(t) \rangle + 1]$. In general, the equation of motion $(\partial/\partial t)\langle \sigma^z \rangle = \text{Tr}[\sigma^z \dot{\rho}]$
 342 depends on both the first order moments $\langle \sigma^{x,y,z} \rangle$ and $\langle a \rangle$ as well as higher order moments,
 343 leading to a hierarchy of coupled equations. Within mean field theory, the second order
 344 moments are factorised as $\langle AB \rangle = \langle A \rangle \langle B \rangle$ which closes the set of equations at first order.
 345 This approximation is valid at large N , as corrections scale as $1/N$. To capture the leading
 346 order effects of finite-sizes we make a second-order cumulant expansion²⁹⁻³¹, i.e. we keep
 347 second-order cumulants $\langle\langle AB \rangle\rangle = \langle AB \rangle - \langle A \rangle \langle B \rangle$ and assume that the third-order
 348 cumulants vanish, which allows us to rewrite third-order moments into products of first
 349 and second-order moments³⁶. In our experiments, the number of molecules in the cavity
 350 is large ($>10^{10}$) and we find higher order correlations are negligible. We give the equations
 351 of motion up to second order in the Supplementary Information.

352 **Operating regimes**

353 The decay-dominated (purple region in Fig. 3a and b) regime occurs when the
 354 collective light-matter coupling is weaker than the decay channels, $g\sqrt{Nr'} < \{\kappa, \gamma^z, \gamma^-\}$,
 355 where $r' = \max(1, r)$. In this regime, the time scale of cavity dynamics is slow relative
 356 to the decay rate. Fig. 3c shows a typical time dependence of the DQB in this regime,

357 indicating how the model parameters affect the dynamics. In this regime, the increase in
 358 the effective coupling relative to the decay strength sees an N^2 superextensive scaling of
 359 the energy and power density, while rise time remains constant. Experiment A3 operates
 360 near the boundary of this regime (Fig. 3a).

361 In the coupling-dominated (green region in Fig. 3a and b) regime, the effective
 362 collective light-matter coupling $g\sqrt{Nr'} > \{\gamma^z, \gamma^-, \kappa\}$, dominates over the decay
 363 channels. In this regime, the time scale of cavity dynamics is fast relative to the decay
 364 rate, and we observe \sqrt{N} -superextensive power scaling and $1/\sqrt{N}$ dependence of rise
 365 time, while the maximum energy density remains constant. While power scaling is
 366 superextensive in both regimes, the origin of this differs: for the decay-dominated regime
 367 this is the result of the superextensive energy scaling, while for the coupling-dominant
 368 regime it is the result of a superextensive decrease in the rise time. Experiments A1 and
 369 A2 operates in this regime (Fig. 3a).

370 In the crossover between the regimes (purple-green), the collective coupling falls
 371 between the cavity decay rate and the TLS dephasing rate, $\{\kappa, \gamma^-\} < g\sqrt{Nr'} < \gamma^z$. In Fig.
 372 3a and b, γ^- is small such that $g\sqrt{Nr'} \gg \gamma^-$ for all values of N , and so there is no
 373 boundary labelled for this decay rate. In this case, capacity and rise-time can
 374 simultaneously scale super- and subextensively, but at a rate slower than in the decay and
 375 coupling-dominated regimes, respectively. Experiments B1 and B2 operate in this regime
 376 (Fig. 3b).

377 **Decay and coupling rates**

378 The parameters needed in the theory calculations are the cavity leakage rate κ , the
 379 dephasing rate γ^z , the non-radiative decay rate γ^- , the interaction strength g , and the

380 temporal width of the instrument response function, σ_R . Note that the temporal width of
 381 the pump pulse is fixed at $\sigma = 20$ fs. Using transfer matrix modelling on the weakly
 382 coupled cavities we estimate that the cavity leakage rate κ is around 2.1 and 2.2 meV for
 383 the 1% and 0.5% cavities respectively. Consistent with this, we used $\kappa = 2$ meV in the
 384 theory calculations for all cavities. Based on the measured finesse of the cavities we
 385 estimate that $\sigma_R = 120$ fs, which we then use in all theory calculations. For the dephasing
 386 rate, we note that as one enters the strong-coupling regime, exciton delocalisation
 387 suppresses the effect of dephasing³⁷. To approximately capture this effect, we assume that
 388 the dephasing rate scales with the number of molecules as $\gamma^z = \gamma_0^z \left(N_{5\%}/N \right)$ where γ_0^z is
 389 taken to be constant and $N_{5\%}$ is the number of molecules in the 5% cavity. The
 390 experimental uncertainty in N is estimated to be 10%.

391 The remaining three parameters in the model (γ_0^z , γ^- , and g) were found through
 392 a global chi-squared optimisation, simultaneously optimising over all experiments.
 393 Uncertainties in these fitting parameters were then estimated by using the reduced $\tilde{\chi}^2$
 394 distribution to find the 68% confidence interval of the model parameters. This
 395 corresponds to the range $\tilde{\chi}^2 \leq \tilde{\chi}_{min}^2 + \Delta$, where for a three parameter optimisation and
 396 k total data points $\Delta \approx 3.51/(k - 3)$.³⁸ From this procedure we found $\gamma^- =$
 397 $(0.0263_{-0.0030}^{+0.0031})$ meV, $g = (16.1_{-1.3}^{+1.0})$ neV and $\gamma_0^z = (1.41_{-0.17}^{+0.19})$ meV. See
 398 Supplementary Information for more details.

399 **Acknowledgements**

400 We thank the U.K. EPSRC for part funding this research via the Programme Grant
 401 ‘Hybrid Polaritonics’ (EP/M025330/1). We also thank the Royal Society for a
 402 International Exchange Grant(IES\R3\170324) ‘Development of BODIPY dyes for

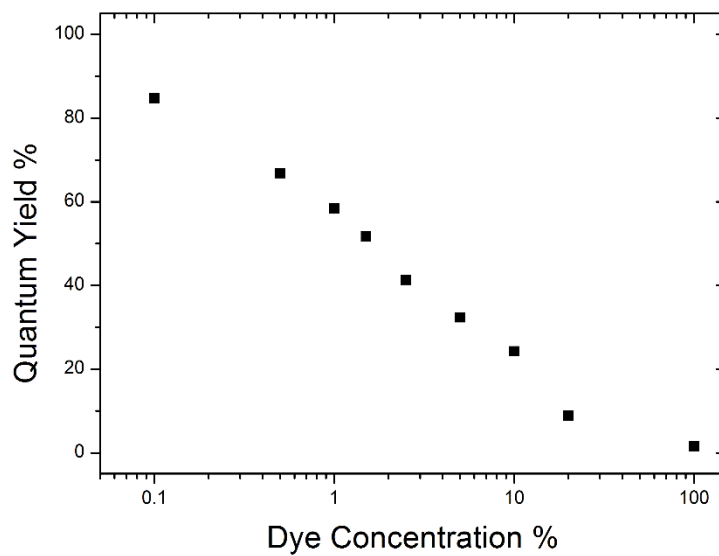
403 strongly coupled microcavities'. K.M. thanks the University of Sheffield for a PhD
 404 studentship via the EPSRC DTG account x/012169-15. D. R. acknowledges studentship
 405 funding from EPSRC under grant no. EP/L015110/1. T.V. and L.G. thank the Regione
 406 Lombardia Funding project IZEB. J.Q.Q. acknowledges the Ramsay fellowship and the
 407 Centre for Nanoscale BioPhotonics Family Friendly Fund, for financial support of this
 408 work. We thank Caspar Clark and Ross Preston at Helia Photonics Ltd for fabricating the
 409 bottom DBRs. We also thank Richard Grant for the measurement of concentration-
 410 dependent photoluminescence quantum-yield of the LFO.

411 References

- 412 1 Alicki, R. & Fannes, M. Entanglement boost for extractable work from
 413 ensembles of quantum batteries. *Phys Rev E* **87** (2013).
- 414 2 Hovhannisyanyan, K. V., Perarnau-Llobet, M., Huber, M. & Acin, A. Entanglement
 415 Generation is Not Necessary for Optimal Work Extraction. *Phys Rev Lett* **111**,
 416 doi:ARTN 240401 10.1103/PhysRevLett.111.240401 (2013).
- 417 3 Binder, F. C., Vinjanampathy, S., Modi, K. & Goold, J. Quantacell: powerful
 418 charging of quantum batteries. *New J Phys* **17**, doi:Artn 075015 10.1088/1367-
 419 2630/17/7/075015 (2015).
- 420 4 Campaioli, F. *et al.* Enhancing the Charging Power of Quantum Batteries. *Phys*
 421 *Rev Lett* **118**, doi:ARTN 150601 10.1103/PhysRevLett.118.150601 (2017).
- 422 5 Cao, J. *et al.* Quantum biology revisited. *Science Advances* **6**, eaaz4888,
 423 doi:10.1126/sciadv.aaz4888 (2020).
- 424 6 Santos, A. C., Saguia, A. & Sarandy, M. S. Stable and charge-switchable
 425 quantum batteries. *Phys Rev E* **101**, 062114, doi:10.1103/PhysRevE.101.062114
 426 (2020).
- 427 7 Quach, J. Q. & Munro, W. J. Using Dark States to Charge and Stabilize Open
 428 Quantum Batteries. *Physical Review Applied* **14**, 024092,
 429 doi:10.1103/PhysRevApplied.14.024092 (2020).
- 430 8 Kippelen, B. & Brédas, J.-L. Organic photovoltaics. *Energy & Environmental*
 431 *Science* **2**, 251-261, doi:10.1039/B812502N (2009).
- 432 9 Mazzio, K. A. & Luscombe, C. K. The future of organic photovoltaics.
 433 *Chemical Society Reviews* **44**, 78-90, doi:10.1039/C4CS00227J (2015).
- 434 10 Hedley, G. J., Ruseckas, A. & Samuel, I. D. W. Light Harvesting for Organic
 435 Photovoltaics. *Chemical Reviews* **117**, 796-837,
 436 doi:10.1021/acs.chemrev.6b00215 (2017).
- 437 11 Cheng, P., Li, G., Zhan, X. & Yang, Y. Next-generation organic photovoltaics
 438 based on non-fullerene acceptors. *Nature Photonics* **12**, 131-142,
 439 doi:10.1038/s41566-018-0104-9 (2018).

- 440 12 Andolina, G. M. *et al.* Charger-mediated energy transfer in exactly solvable
441 models for quantum batteries. *Phys Rev B* **98**, doi:ARTN 205423
442 10.1103/PhysRevB.98.205423 (2018).
- 443 13 Andolina, G. M. *et al.* Extractable Work, the Role of Correlations, and
444 Asymptotic Freedom in Quantum Batteries. *Phys Rev Lett* **122**, doi:ARTN
445 047702 10.1103/PhysRevLett.122.047702 (2019).
- 446 14 Alicki, R. A quantum open system model of molecular battery charged by
447 excitons. *J Chem Phys* **150**, doi:Artn 214110 10.1063/1.5096772 (2019).
- 448 15 Zhang, Y. Y., Yang, T. R., Fu, L. B. & Wang, X. G. Powerful harmonic
449 charging in a quantum battery. *Phys Rev E* **99**, doi:ARTN 052106
450 10.1103/PhysRevE.99.052106 (2019).
- 451 16 Quach, J. Q. & Munro, W. J. Using dark states to charge and stabilise open
452 quantum batteries. *arXiv:2002.10044 [quant-ph]* (2020).
- 453 17 Le, T. P., Levinsen, J., Modi, K., Parish, M. M. & Pollock, F. A. Spin-chain
454 model of a many-body quantum battery. *Phys Rev A* **97**, doi:ARTN 022106
455 10.1103/PhysRevA.97.022106 (2018).
- 456 18 Zhang, X. & Blauboer, M. Enhanced energy transfer in a Dicke quantum
457 battery. *arXiv:1812.10139 [quant-ph]* (2018).
- 458 19 Ferraro, D., Campisi, M., Andolina, G. M., Pellegrini, V. & Polini, M. High-
459 Power Collective Charging of a Solid-State Quantum Battery. *Phys Rev Lett*
460 **120**, doi:ARTN 117702 10.1103/PhysRevLett.120.117702 (2018).
- 461 20 Gross, M. & Haroche, S. Superradiance: An essay on the theory of collective
462 spontaneous emission. *Physics Reports* **93**, 301-396, doi:10.1016/0370-
463 1573(82)90102-8 (1982).
- 464 21 Higgins, K. D. B. *et al.* Superabsorption of light via quantum engineering. *Nat*
465 *Commun* **5**, 4705, doi:10.1038/ncomms5705 (2014).
- 466 22 Higgins, K. D. B., Lovett, B. W. & Gauger, E. M. Quantum-Enhanced Capture
467 of Photons Using Optical Ratchet States. *The Journal of Physical Chemistry C*
468 **121**, 20714-20719, doi:10.1021/acs.jpcc.7b07138 (2017).
- 469 23 Sanvitto, D. & Kéna-Cohen, S. The road towards polaritonic devices. *Nature*
470 *Materials* **15**, 1061-1073, doi:10.1038/nmat4668 (2016).
- 471 24 Savona, V., Andreani, L. C., Schwendimann, P. & Quattropani, A. Quantum
472 well excitons in semiconductor microcavities: Unified treatment of weak and
473 strong coupling regimes. *Solid State Commun* **93**, 733-739, doi:10.1016/0038-
474 1098(94)00865-5 (1995).
- 475 25 Cerullo, G., Manzoni, C., Lürer, L. & Polli, D. Time-resolved methods in
476 biophysics. 4. Broadband pump-probe spectroscopy system with sub-20 fs
477 temporal resolution for the study of energy transfer processes in photosynthesis.
478 *Photochemical & Photobiological Sciences* **6**, 135-144, doi:10.1039/B606949E
479 (2007).
- 480 26 Manzoni, C. & Cerullo, G. Design criteria for ultrafast optical parametric
481 amplifiers. *Journal of Optics* **18**, 103501, doi:10.1088/2040-8978/18/10/103501
482 (2016).
- 483 27 Svelto, O. & Hanna, D. C. *Principles of lasers*. Vol. 1 (Springer, 2010).
- 484 28 Virgili, T. *et al.* An ultrafast spectroscopy study of stimulated emission in
485 poly(9,9-dioctylfluorene) films and microcavities. *Appl Phys Lett* **74**, 2767-
486 2769, doi:10.1063/1.124008 (1999).

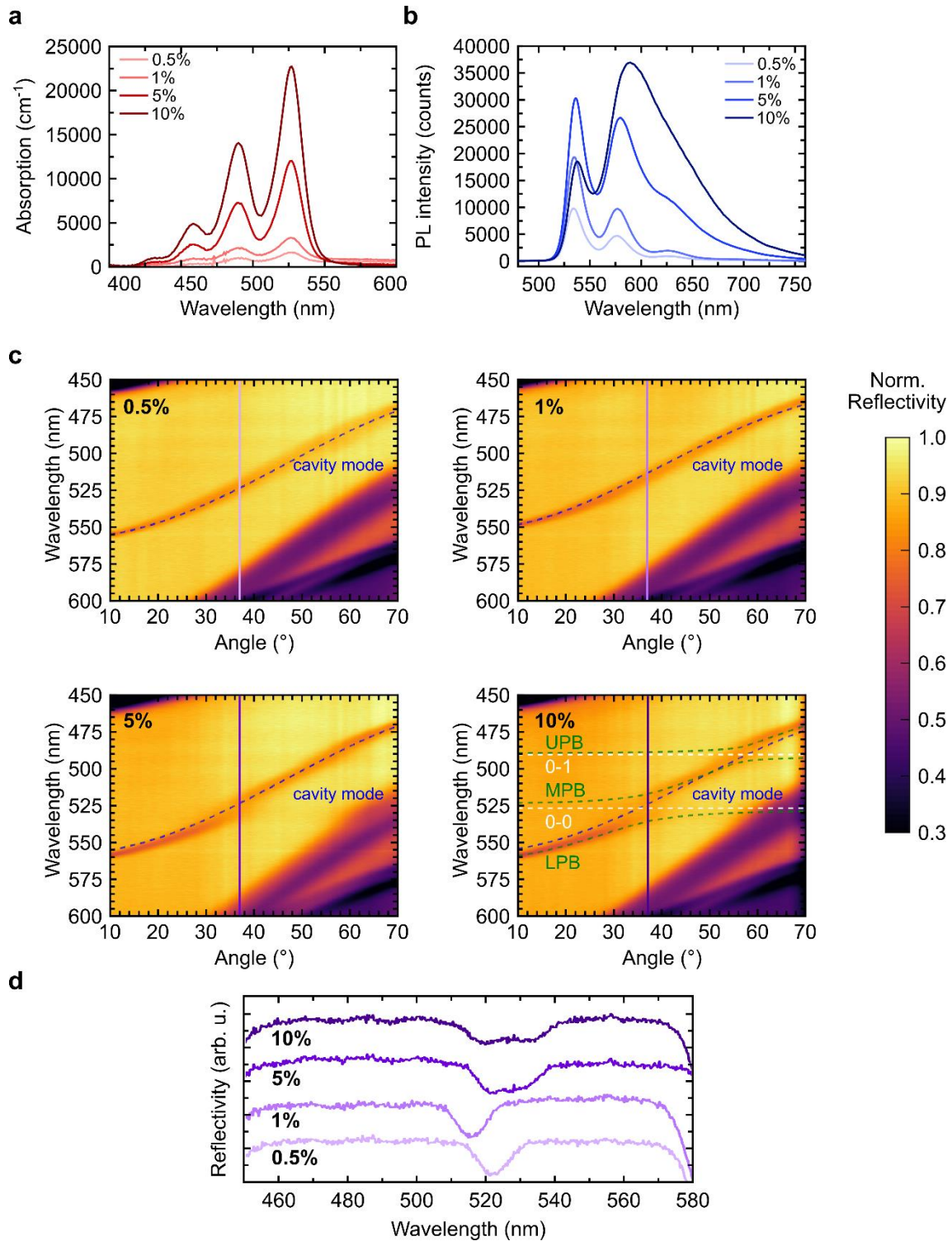
- 487 29 Kirton, P. & Keeling, J. Suppressing and Restoring the Dicke Superradiance
488 Transition by Dephasing and Decay. *Phys Rev Lett* **118**, 123602,
489 doi:10.1103/PhysRevLett.118.123602 (2017).
- 490 30 Arnardottir, K. B., Moilanen, A. J., Strashko, A., Törmä, P. & Keeling, J.
491 Multimode Organic Polariton Lasing. *arXiv:2004.06679* (2020).
- 492 31 Zens, M., Krimer, D. O. & Rotter, S. Critical phenomena and nonlinear
493 dynamics in a spin ensemble strongly coupled to a cavity. II. Semiclassical-to-
494 quantum boundary. *Phys Rev A* **100**, 013856,
495 doi:10.1103/PhysRevA.100.013856 (2019).
- 496 32 Brown, W. M. & Gauger, E. M. Light Harvesting with Guide-Slide
497 Superabsorbing Condensed-Matter Nanostructures. *The Journal of Physical*
498 *Chemistry Letters* **10**, 4323-4329, doi:10.1021/acs.jpcllett.9b01349 (2019).
- 499 33 Yang, D. *et al.* Observation of superabsorption by correlated atoms.
500 *arXiv:1906.06477* (2019).
- 501 34 Hecht, E. *Optics*. (Pearson Education, Incorporated, 2017).
- 502 35 Wang, L. V. & Wu, H.-i. *Biomedical optics: principles and imaging*. (John
503 Wiley & Sons, 2012).
- 504 36 Gardiner, C. Handbook of stochastic methods for physics, chemistry, and the
505 natural sciences Springer. *Berlin (4th Ed)* (2009).
- 506 37 Pino, J. d., Feist, J. & Garcia-Vidal, F. J. Quantum theory of collective strong
507 coupling of molecular vibrations with a microcavity mode. *New J Phys* **17**,
508 053040, doi:10.1088/1367-2630/17/5/053040 (2015).
- 509 38 Wall, J. V. & Jenkins, C. R. *Practical Statistics for Astronomers*. (Cambridge
510 University Press, 2003).
511

512 **Extended Data Figures**

513

514 **Extended Data Figure 1:** Photoluminescence quantum yield as function of LFO concentration.

515

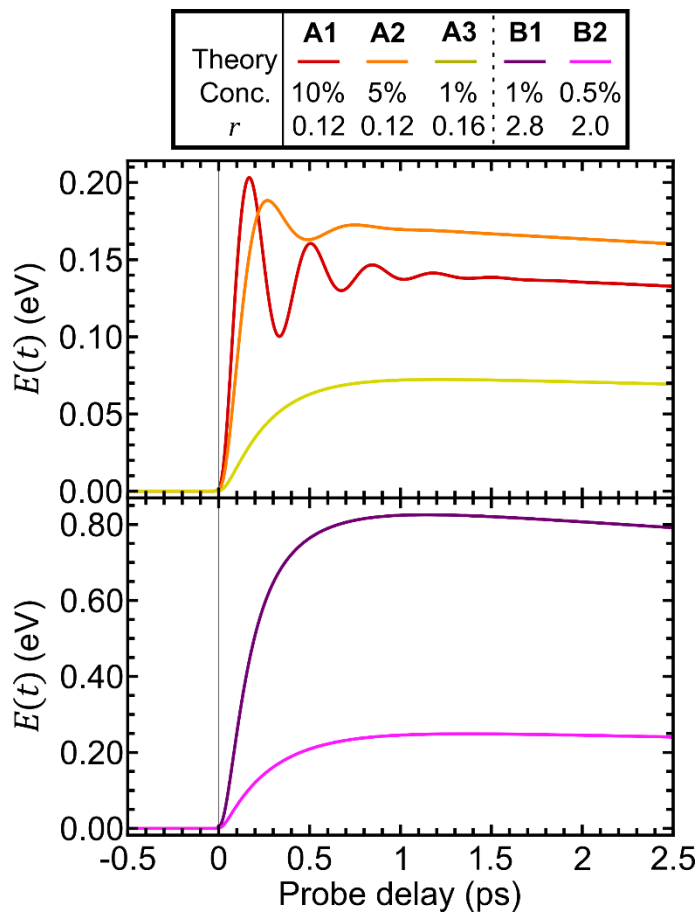


516

517

518 **Extended Data Figure 3: Absorption, photoluminescence of the LFO films and reflectivity**519 **spectra of the quantum battery microcavities. (a) Absorption and (b) photoluminescence**520 **spectra for the 0.5%,1%,5%, and 10% LFO-concentration films. (c) Reflectivity spectra for**

521 0.5%,1%,5%, and 10% LFO-concentration microcavities. UPB, MPB, and LPB label the upper,
522 middle, and lower polariton branches, respectively. Also indicated are the 0-0 and 0-1 transition
523 wavelengths. **(d)** is a slice of the reflectivity spectra at 37° . The single dip in the 0.5% and 1%
524 concentration spectra indicate the weak-coupling regime. The double dip seen in the 10%
525 concentration spectra, represent the polaritonic states, indicating th strong-coupling regime. The
526 5% concentration spectrum represents a situation intermediate between a single and double dip,
527 indicating an intermediate-coupling regime.
528



529

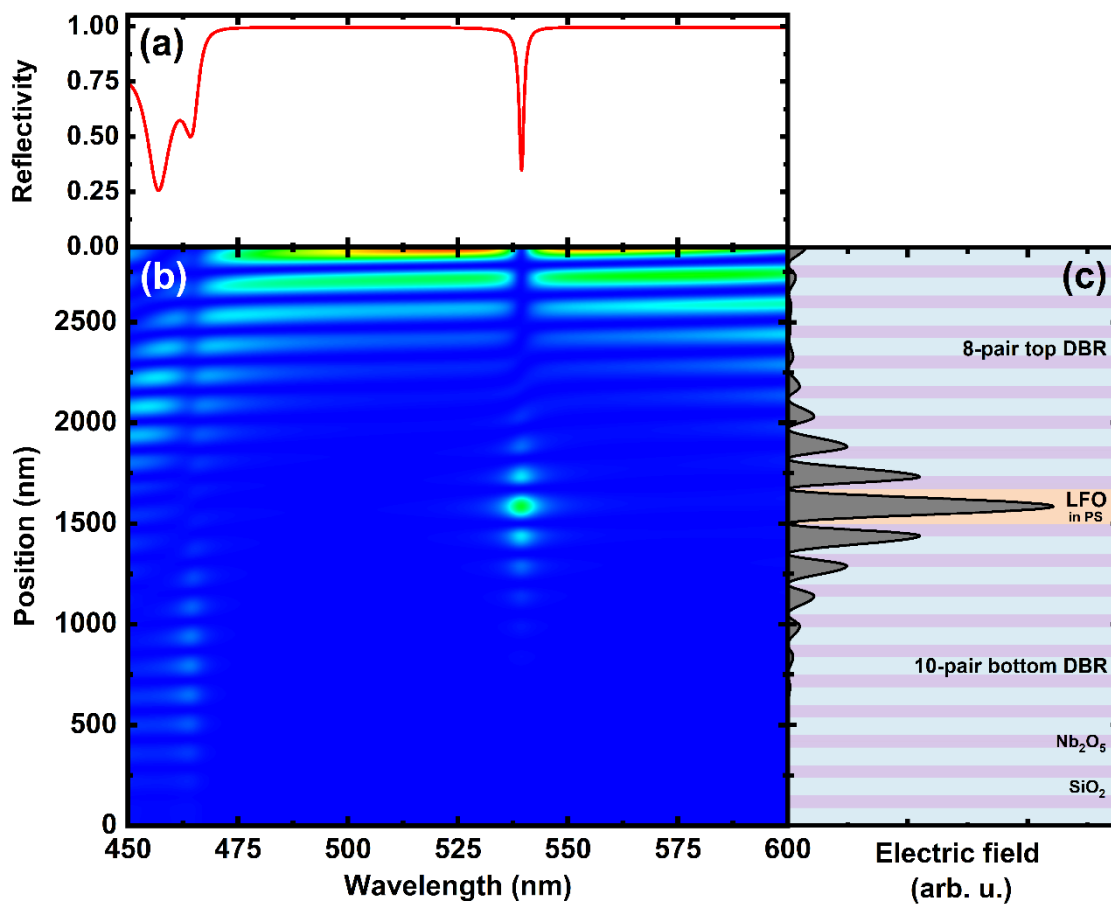
530 **Extended Data Figure 2:** Energetics of the quantum batteries without convolution by the

531

instrument response function.

532

533



534

535

536 **Extended Data Figure 4: Transfer matrix simulation of the electric field distribution for the**537 **1% cavity. (a)** shows the cavity reflectivity, **(b)** the spectrally-resolved electric field amplitude,538 and **(c)** the electric field amplitude at the cavity mode wavelength. The shaded sections of **(c)**539 indicate the different materials which make up the cavity, with Nb₂O₅ in purple (refractive index,540 $n = 2.25$), SiO₂ in blue ($n = 1.52$), and LFO in PS in orange ($n = 1.60$). All simulations were made

541 using transfer matrix modelling at an angle of 20° to the cavity normal to maintain consistency

542 with the transient reflectivity measurements.

543

Exp.	$N [\times 10^{10}]$	τ [ps]	E_{max} [eV]	P_{max} [eV/ps]
A1	16	0.08	0.20	1.94
A2	8.1	0.11	0.19	1.20
A3	1.6	0.21	0.07	0.21
B1	1.6	0.16	0.83	3.31
B2	0.8	0.21	0.25	0.75

544 **Extended Data Table 1: Summary of the experimental results.** In experimental groupings A1,
545 A2, A3 and B1, B2, the number of molecules (N) increase whilst the ratio of photons to molecules
546 remains constant ($r \approx 0.14$ and 2.4 respectively). The rise time τ , is the time to reach $E_{max}/2$.
547 The battery capacity E_{max} , is the peak stored energy per molecule or energy density. The battery
548 charging rate $P_{max} = \max(dE / dt)$, is the peak charging power per molecule or charging
549 power density.

Figures

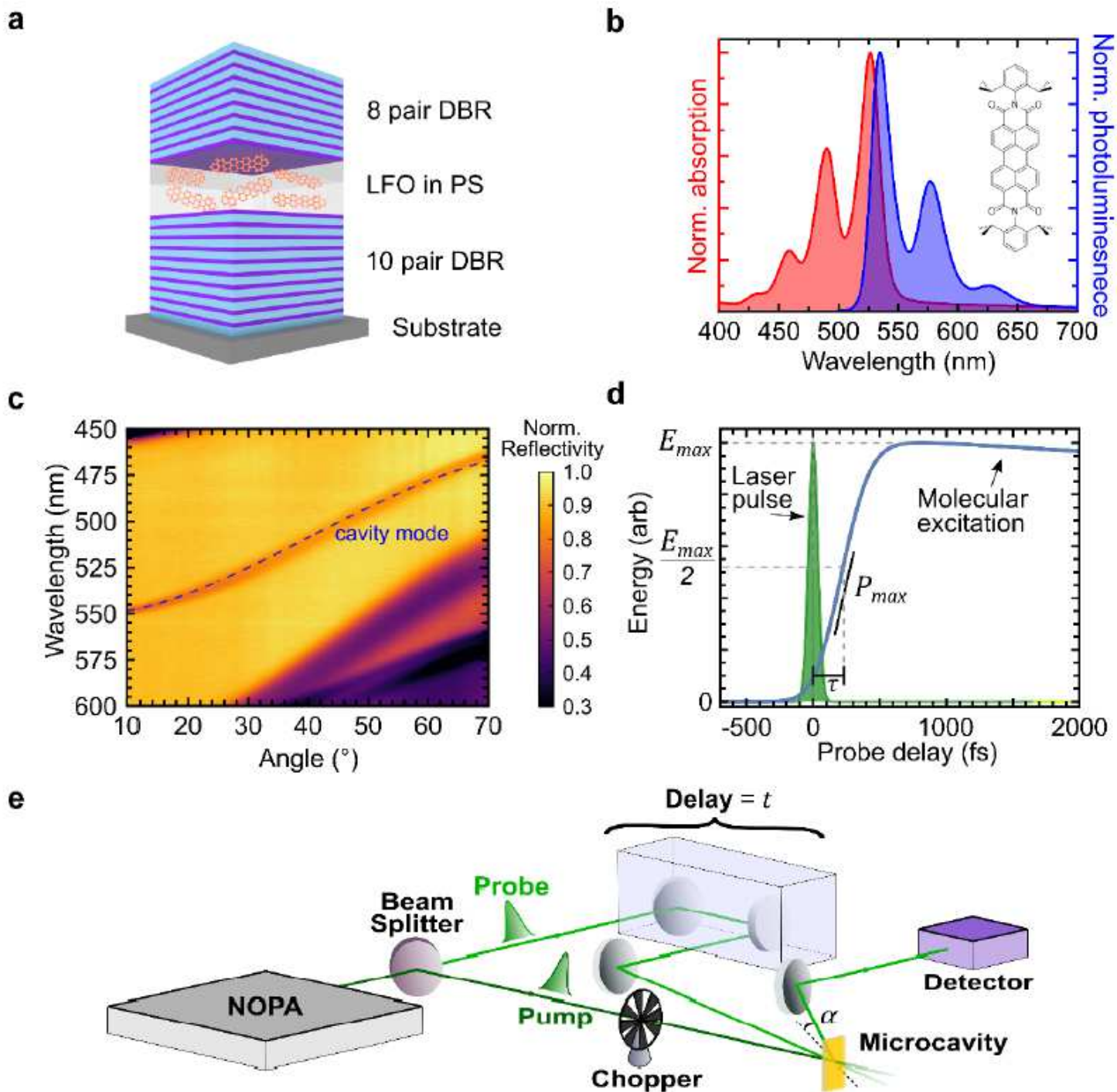
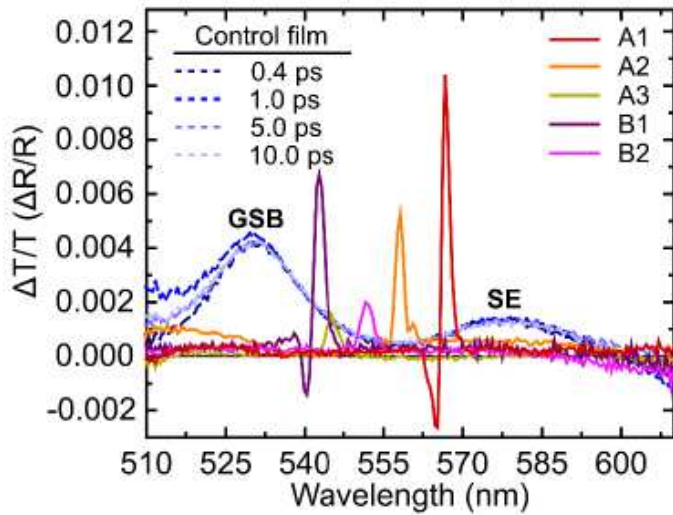


Figure 1

Schematics of the LFO microcavity and experimental setup. (a) Microcavity consisting of Lumogen-F Orange (LFO) dispersed in a polystyrene (PS) matrix between distributed Bragg reflectors (DBRs). (b) Normalised absorption (red) and photoluminescence (blue) spectra for 1% concentration LFO film, with the molecular structure shown in the inset. We operate near peak absorption/photoluminescence. (c) Angle-dependent reflectivity of the 1% cavity, with a fit for the cavity mode shown by the blue dashed line.

(d) A laser pump pulse excites the LFO molecules. The energetics of the molecules are then measured with probe pulses delayed by time t , from which we can ascertain the peak energy density (Φ_{max}), rise time (τ_r), and peak charging power (Φ_{max}). (e) The experimental setup for ultrafast transient reflectivity measurements. The output of a non-collinear optical parametric amplifier (NOPA) is split to generate pump (dark green) and probe (light green) pulses. A mechanical chopper is used to modulate the pump pulse to produce alternating pump-probe and probe-only pulses.

a



b

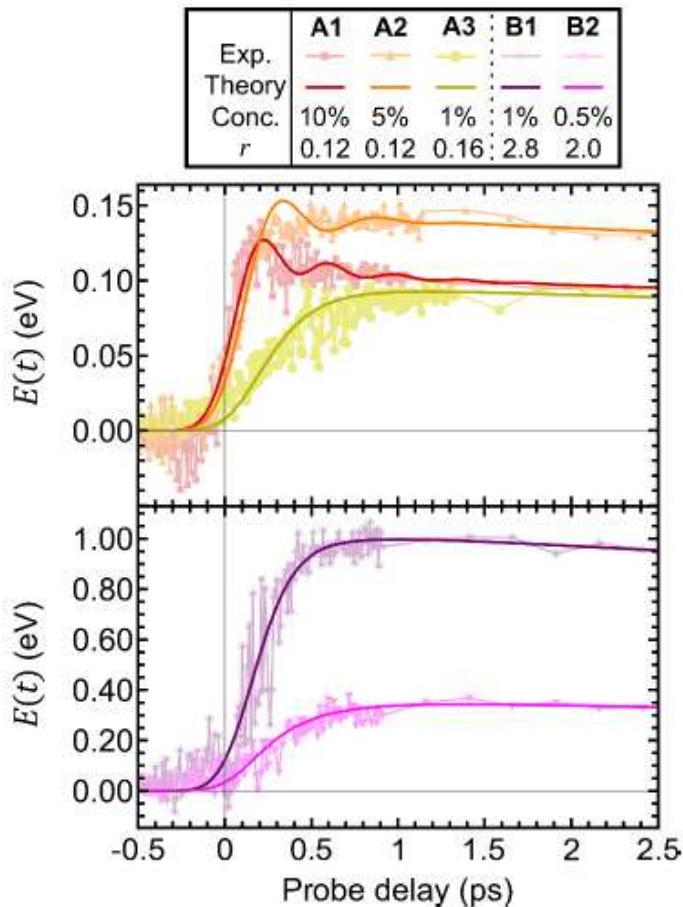


Figure 2

Experimental demonstration of the superextensive charging of the Dicke quantum battery. (a) Differential-transmittivity ($\Delta T/T$) spectra for the control film at various probe delay times, and the differential-reflectivity ($\Delta R/R$) spectra for the DQBs at 1.25 ps probe delay. (b) Temporally resolved energy density of the DQBs. A1, A2 and A3 label results for DQBs containing LFO at concentrations of 10%, 5% and 1%, as the ratio of pump photons to molecules is kept approximately constant at $r \approx 0.14$. B1 and B2 label measurements for LFO at concentrations of 1% and 0.5%, with $r \approx 2.4$. The use of two different r values was necessary to achieve a sufficiently high-signal-to-noise ratio. Points mark the experimental data, while continuous solid lines are the results of the theoretical model.

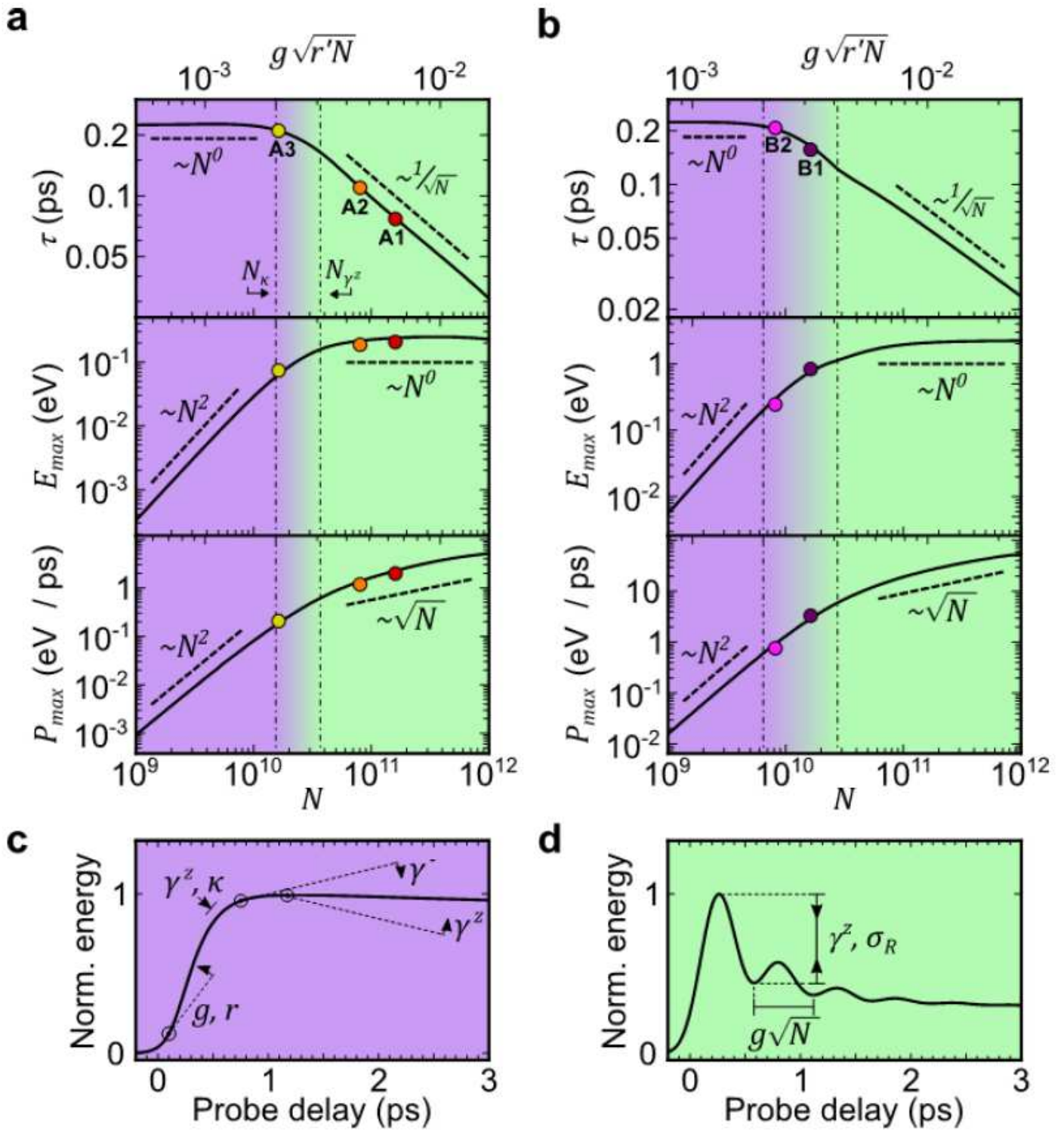


Figure 3

Operating regimes of the quantum batteries. (a) and (b) show the theoretical model (solid line) for $\eta = 1.4$ and 2.4 , respectively. We show three operating regimes: decay-dominated (purple), coupling-dominated (green), and a decay-coupling-crossover regime. The decay-dominated regime is bounded by $\eta < 2/\eta'$, and the coupling-dominated regime is bounded by $\eta > 2/\eta'$, where $\eta' = \max(1, \eta)$. The coloured dots indicate where the experiments sit on these curves. The uncertainty in N is 10%, which is smaller than the

dot size. (c) qualitatively depicts the effects of the model parameters in shaping the dynamics in the decay-dominated regime. (d) qualitatively depicts the effects of the additional model parameters in shaping the dynamics in the coupling-dominated regimes.

Supplementary Files

This is a list of supplementary files associated with this preprint. Click to download.

- [FinalMovie.mov](#)
- [OrganicQBSupplementarysubmitted.pdf](#)